

X-ray spectropolarimetry of the bright atoll Serpens X-1

F. Ursini¹, A. Gnarini¹, S. Bianchi¹, A. Bobrikova², F. Capitanio³, M. Cocchi⁴, S. Fabiani³, R. Farinelli⁵, P. Kaaret⁶,
G. Matt¹, M. Ng⁷, J. Poutanen², S. Ravi⁷, and A. Tarana³

¹ Dipartimento di Matematica e Fisica, Università degli Studi Roma Tre, via della Vasca Navale 84, 00146 Roma, Italy
e-mail: francesco.ursini@uniroma3.it

² Department of Physics and Astronomy, FI-20014 University of Turku, Finland

³ INAF Istituto di Astrofisica e Planetologia Spaziali, Via del Fosso del Cavaliere 100, 00133 Roma, Italy

⁴ INAF Osservatorio Astronomico di Cagliari, via della Scienza 5, I-09047 Selargius (CA), Italy

⁵ INAF Osservatorio di Astrofisica e Scienza dello Spazio di Bologna, Via P. Gobetti 101, I-40129 Bologna, Italy

⁶ NASA Marshall Space Flight Center, Huntsville, AL 35812, USA

⁷ MIT Kavli Institute for Astrophysics and Space Research, Massachusetts Institute of Technology, Cambridge, MA 02139, USA

Received ...; accepted ...

ABSTRACT

We present simultaneous X-ray polarimetric and spectral observations of the bright atoll source Ser X-1 carried out with the Imaging X-ray Polarimetry Explorer (IXPE), NICER, and *NuSTAR*. We obtain an upper limit of 2% (99% confidence level) on the polarization degree in the 2–8 keV energy band. We detect four type-I X-ray bursts, two of which during the IXPE observation. This is the first time that has IXPE observed type-I X-ray bursts, and it allows us to place an upper limit on their polarization degree; however, due to the limited total number of counts in each burst, we obtain a relatively high upper limit (80%). We confirm the presence of reflection features in the X-ray spectrum, notably a broad iron line. Fitting the data with a relativistic reflection model, we derive a disk inclination of 25°. The spectral and polarization properties are comparable with other atolls observed by IXPE, suggesting a similar accretion geometry, and the relatively low polarization is consistent with the low inclination.

Key words. polarization – stars: neutron – X-rays: binaries – X-rays: individual: Ser X-1

1. Introduction

Accreting, weakly magnetized neutron star low-mass X-ray binaries (NS-LMXBs) are very bright X-ray sources and excellent laboratories for studying the physics of accretion onto compact objects. They are divided into two main classes, Z and atoll, according to the pattern they trace on X-ray color-color diagrams (Hasinger & van der Klis 1989). Atoll sources are also less luminous and tend to have weaker magnetic fields than Z sources. The X-ray spectrum of NS-LMXBs is generally well described by a soft thermal component plus a hard Comptonization component, but their physical origin is still uncertain. The soft component could be due to either the accretion disk or the NS, while the hard component could originate in a hot corona, in a boundary layer (BL) between the disk and the NS (Popham & Sunyaev 2001), or in a spreading layer (SL) around the NS (Inogamov & Sunyaev 1999).

Thanks to X-ray polarimetric results from the Imaging X-ray Polarimetry Explorer (IXPE; Weisskopf et al. 2022; Soffitta et al. 2021), our understanding of NS-LMXBs is advancing significantly. So far, IXPE has detected significant polarization in at least eight NS-LMXBs, both atoll and Z sources (Farinelli et al. 2023; Cocchi et al. 2023; Jayasurya et al. 2023; Chatterjee et al. 2023; Ursini et al. 2023; Di Marco et al. 2023a; Fabiani et al. 2024; Saade et al. 2024; La Monaca et al. 2024; Bobrikova et al. 2024), plus one stringent upper limit (Capitanio et al. 2023). Detailed spectropolarimetric analysis has revealed that the hard component dominates the polarization signal, while the soft emission has a low polarization (Farinelli et al. 2023; Cocchi et al. 2023; Ursini et al. 2023; Di Marco et al. 2023a;

La Monaca et al. 2024). The results so far suggest that the soft thermal component is due to the accretion disk, while Comptonization likely takes place in a BL or SL. In principle, reflection off the disk surface can significantly contribute to the observed polarization (Lapidus & Sunyaev 1985). However, it is still unclear whether the reflected component is the dominant contributor (Ursini et al. 2023; Fabiani et al. 2024; Saade et al. 2024). For example, in the case of the atoll source GX 9+9, the observed polarization is likely a combination of Comptonization and reflection (Ursini et al. 2023). Interestingly, IXPE measured surprisingly large polarization in other atolls in the soft state, up to $6\% \pm 2\%$ in the 6–8 keV band in 4U 1624–49 (Saade et al. 2024) and $10\% \pm 2\%$ in the 7–8 keV band in 4U 1820–30 (Di Marco et al. 2023a). These values are much higher than expected for any plausible BL or SL geometry (Gnarini et al. 2022; Capitanio et al. 2023; Farinelli et al. 2024). A possible explanation for the high polarization is a slab-like accretion disk corona or a strong contribution due to scattering off the disk or a wind (Saade et al. 2024).

Serpens X-1 (Ser X-1) is a bright, persistent atoll NS-LMXB. It is a well-studied source, consistently observed in the high luminosity, soft spectral (“banana”) state (e.g., Oosterbroek et al. 2001; Masetti et al. 2004; Cackett et al. 2008; Chiang et al. 2016a; Matranga et al. 2017; Ludlam et al. 2018; Mondal et al. 2020). The occurrence of type-I X-ray bursts is well established in this source (Sztajno et al. 1983; Balucinska & Czerny 1985; Galloway et al. 2008). From observations with the Rossi X-ray Timing Explorer (RXTE), Galloway et al. (2008) found evidence of photospheric radius-expansion bursts, and from their

Table 1. Log of the IXPE and NICER observations.

Satellite	Obs. Id.	Start time (UTC)	Net exp. (ks)
IXPE	03003901	2024-04-15T00:03:51	37.3
NICER	7700020102	2024-04-14T18:36:45	7.8
<i>NuSTAR</i>	91001316002	2024-04-15T08:51:09	33.8

peak luminosity they estimated a distance of 7.7 ± 0.9 kpc. The X-ray spectrum shows both a relativistically broadened Fe $K\alpha$ emission line (Bhattacharyya & Strohmayer 2007; Cackett et al. 2008, 2010; Miller et al. 2013; Chiang et al. 2016a,b) and a Compton reflection hump at 10–20 keV (Miller et al. 2013; Matranga et al. 2017; Ludlam et al. 2018; Mondal et al. 2020). Optical spectroscopy indicates that the Ser X-1 system has a low binary inclination, less than 10° (Cornelisse et al. 2013). Different values of the disk inclination, between $\sim 10^\circ$ and $\sim 50^\circ$, have been reported based on X-ray reflection spectroscopy (Bhattacharyya & Strohmayer 2007; Miller et al. 2013; Matranga et al. 2017; Ludlam et al. 2018; Mondal et al. 2020). In any case, Ser X-1 is one of the X-ray-brightest atolls known (Asai et al. 2022) and thus an excellent target for X-ray polarimetry. In this paper we report on the first IXPE observation of this source, performed jointly with the Neutron Star Interior Composition Explorer (NICER) and *NuSTAR*.

The paper is structured as follows. In Sect. 2 we describe the observations and data reduction. In Sect. 3 we present the X-ray spectropolarimetric analysis. In Sect. 4 we discuss the results and the main conclusions.

2. Observations and data reduction

IXPE observed Ser X-1 on 2024 April 14 with its three detector units (DUs)/mirror module assemblies (MMAs), for a net exposure time of 37.3 ks (Table 1). We produced cleaned level 2 event files using standard filtering criteria with the dedicated `FTOOLS` (v6.33) tasks¹ and the latest calibration files (CALDB 20240125) and response matrices (v13). We extracted the Stokes I , Q , and U spectra from circular regions with a radius of $120''$. We did not subtract the background, following the prescription by Di Marco et al. (2023b) for bright sources. However, we verified that background subtraction does not significantly alter the results; in particular, the polarimetric measurements are not affected at all. We performed the data analysis following the weighted scheme `NEFF` (Baldini et al. 2022; Di Marco et al. 2022). Given the source brightness, each energy bin of the flux (I) spectra contains more than 40 counts, ensuring the applicability of the χ^2 statistics. Thus, we did not re-bin the I spectra but did apply a constant energy binning of 0.2 keV for Q and U Stokes spectra. We fitted the I , Q , and U Stokes spectra from the three DU/MMAs independently.

NICER performed two observations of the source with continuous exposure in the period 2024 April 14–15 simultaneously with IXPE, for a net exposure time of 7.8 ks. The NICER data were reduced using `FTOOLS` tasks and the processing script `NICERL2` to apply standard screening and calibration (CALDB 20240206). We used the data in the 1.5–10 keV band.

NuSTAR (Harrison et al. 2013) observed the source with its X-ray telescopes on Focal Plane Module A (FPMA) and B

¹ https://heasarc.gsfc.nasa.gov/docs/ixpe/analysis/IXPE-SOC-DOC-009D_UG-Software.pdf

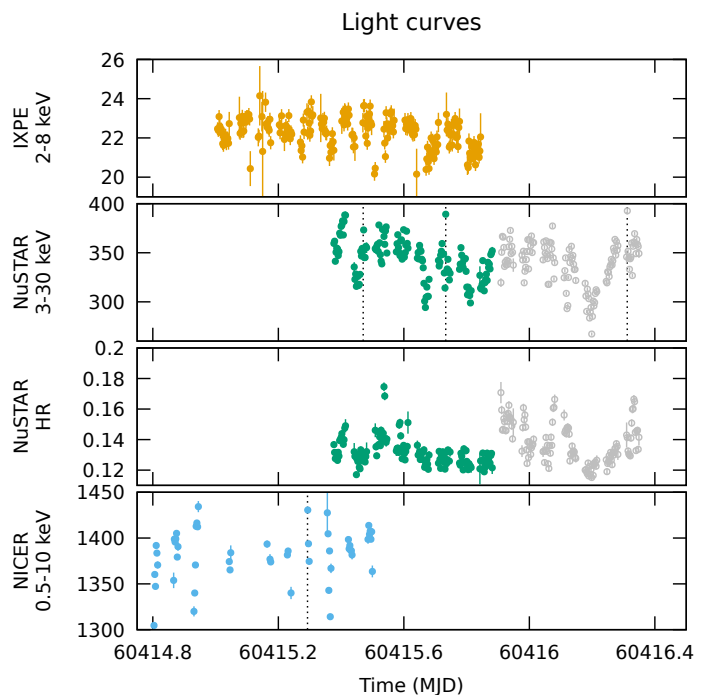


Fig. 1. IXPE, *NuSTAR*, and NICER light curves of Ser X-1 (count s^{-1}). The third panel shows the *NuSTAR* hardness ratio, (10–30 keV)/(3–10 keV). Time bins of 200 s are used. Empty gray circles denote the *NuSTAR* points not simultaneous with the IXPE exposure. Dotted lines mark the type-I bursts.

(FPMB), with a net exposure of 33.8 ks and an overlap with the last ~ 4 hr of the IXPE exposure. We produced cleaned event files with the standard `nupipeline` task and the latest calibration files (CALDB 20240325). The *NuSTAR* background is not negligible at all energies, and thus we performed background subtraction as follows. For both detectors, the background was extracted from a circular region with a standard radius of $60''$. The source radius was set to $120''$ following a procedure that maximizes the signal-to-noise ratio (Piconcelli et al. 2004). Finally, we rebinned the spectra with the standard task `ftgrouppha` with the optimal scheme by Kaastra & Bleeker (2016), also requiring a minimum signal-to-noise of 3 in each bin. The FPMA and FPMB spectra were fitted independently and not co-added. We used the data in the 3–30 keV range since the background starts dominating above 30 keV.

3. Data analysis

3.1. Timing properties

The X-ray flux of Ser X-1 displays a quasiperiodic modulation on a timescale of decades (Asai et al. 2022). However, the recent light curve of the Monitor of All-sky X-ray Image (MAXI; Matsuoka et al. 2009) shows only a limited amplitude variability.

The 200-second-binned light curves obtained with IXPE, NICER, and *NuSTAR* are shown in Fig. 1. The flux variability is apparent, albeit not dramatic. However, some spectral variability is also observed. In particular, the *NuSTAR* hardness, (10–30 keV)/(3–10 keV), changes more rapidly during the second half of the *NuSTAR* exposure, right after the end of the IXPE exposure. Thus, for the sake of the joint spectropolarimetric fit, we only used the NICER and *NuSTAR* data that were taken simultaneously with the IXPE exposure.

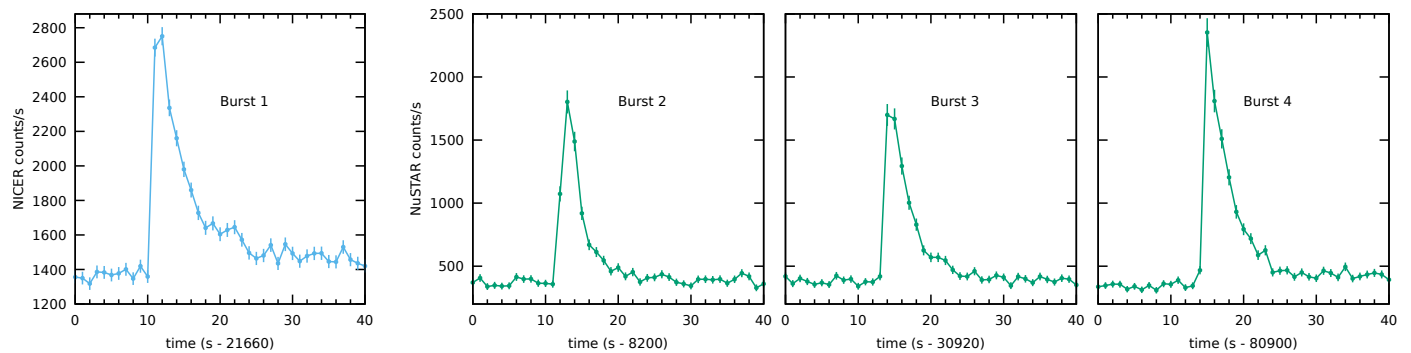


Fig. 2. Profiles of the four type-I X-ray bursts detected with NICER (left panel) and *NuSTAR* (right panels). The first two occurred during the IXPE exposure.

We also constructed 1-second-binned light curves to search for X-ray bursts. We found clear evidence for four type-I X-ray bursts, one observed with NICER and the other three with *NuSTAR*. These four bursts are plotted in Fig. 2. The recurrence times of the bursts are irregular, between 4.5 and 13 hours, consistent with past observations of the source (Sztajno et al. 1983; Galloway et al. 2008). Only the first and second bursts occurred during the IXPE exposure. The third burst occurred during a gap between IXPE observation segments, and the fourth burst occurred after the end of the IXPE exposure. All bursts are well described by a fast rise and exponential decay profile, with an e-folding decay time of 3–4 s (see also Galloway et al. 2008).

We investigated the differences between burst and non-burst emission as follows. We extracted the burst and non-burst data for each instrument; since the IXPE data alone do not provide a sufficient signal-to-noise to identify the bursts, we defined the IXPE good time intervals (GTIs) from the NICER and *NuSTAR* light curves. In other words, for IXPE we extracted the data of the first and second bursts using the NICER and *NuSTAR* GTIs. For each burst, the GTIs were created in 10-second intervals starting from the burst onsets, as determined from the light curves (Fig. 2). For the polarimetric analysis, we extracted a single burst spectrum, combining the two intervals. We note that these two bursts have similar profile and spectral parameters (see also Appendix A). In the following step, we analyzed the Stokes parameters for the whole IXPE exposure, the non-burst period, and the bursts.

3.2. Polarimetric analysis

We first performed a polarimetric analysis of the whole IXPE observation (i.e., not separating burst and non-burst periods). The normalized Stokes parameters measured by IXPE in the source region are plotted in Fig. 3, together with the minimum detectable polarization (MDP) at the 99% level. We do not obtain a significant detection, with an upper limit to the 2–8 keV polarization degree (PD) of 2% at the 99% confidence level (one degree of freedom)². We do not observe any significant evolution with energy. In Table 2 we report the PD measured in different energy bands with *xSPEC* 12.14.0 (Arnaud 1996). In Fig. 4 we plot the two-dimensional contours of the PD and polarization angle (PA) measured with *xSPEC*. The statistical significance is around 68% in the whole 2–8 keV band and increases up to 90% when considering just the 4–8 keV band, however not enough

² The quoted upper limits on the PD are derived from the one-dimensional error, i.e., independent of the value of the PA.

Table 2. PD and PA measured with *xSPEC*.

Energy range (keV)	PD (%)	PD U.L. (%)	PA (°)
2–8	0.8 ± 0.4	< 2.0	-60 ± 15
2–4	0.5 ± 0.5	< 1.9	-
4–8	1.9 ± 0.8	< 4.0	-64 ± 12

Notes. Uncertainties are given at the 68% (1σ) confidence level for one parameter of interest; upper limits are quoted at the 99% confidence level.

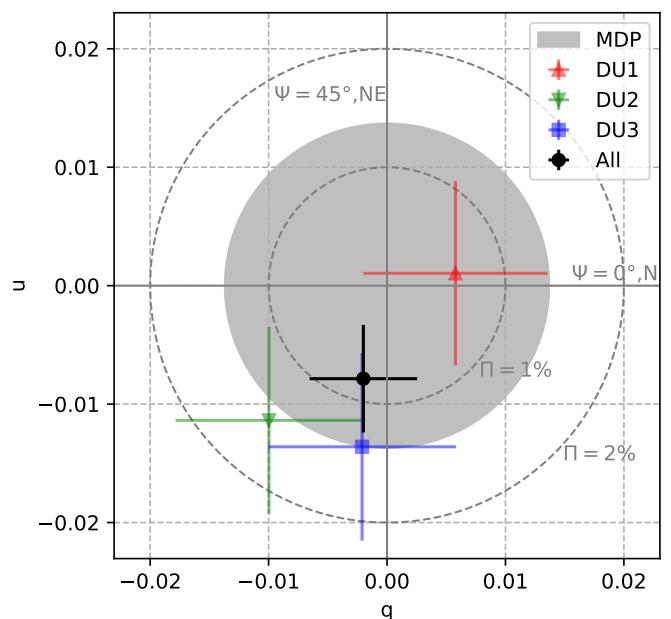


Fig. 3. Normalized Stokes q and u parameters in the 2–8 keV band for the three IXPE DUs and their combination. The gray-filled circle encloses the 99% MDP.

to warrant a detection claim. We obtain consistent values from the polarization cubes extracted with IXPEOBSSIM (Baldini et al. 2022).

We also performed a similar analysis of the IXPE data of the burst phases. Since the exposure amounts to just 20 s, the MDP is 80%, and the upper limit to the burst polarization is on the same order.

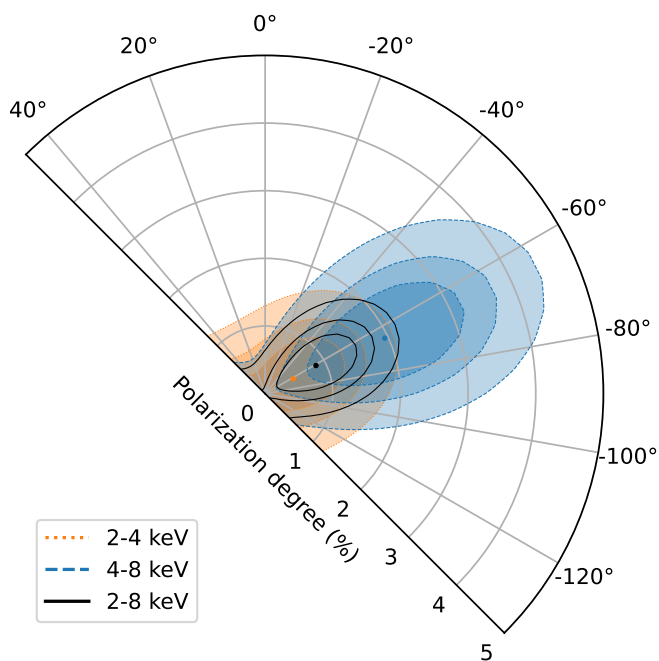


Fig. 4. Contour plots of the PD and PA at the 68, 90, and 99% confidence levels, in the 2–4 keV (dotted orange), 4–8 keV (dashed blue), and 2–8 keV (solid black) energy bands. Color transparency increases with increasing confidence level.

3.3. Spectropolarimetric analysis

We performed a joint fit of IXPE, NICER, and *NuSTAR* spectropolarimetric data with *xSPEC*. Here we focus on the stationary (non-burst) phase; the spectra of the bursts are discussed in Appendix A. To take interstellar absorption into account, we always included the *tbabs* model (Wilms et al. 2000), leaving the column density as a free parameter. We included cross-calibration constants, and we also applied a gain correction to the IXPE and NICER spectra using the *gain fit* command in *xSPEC* to account for the imperfect spectral agreement between the different instruments. We also found some residuals in the NICER spectrum below 2 keV, likely due to calibration issues³ (see also Fabiani et al. 2024), and we included an absorption edge to account for them.

First, we fitted the IXPE, NICER, and *NuSTAR* spectra with a model consisting of two components: a disk multicolor blackbody (*diskbb* in *xSPEC*; Mitsuda et al. 1984) and a Comptonized blackbody (*bbodyrad* convolved with *thcomp*; Zdziarski et al. 2020). The model was multiplied by a constant polarization via *polconst*. This fit is, however, unacceptable, as the NICER and *NuSTAR* residuals clearly show the presence of a strong iron line and Compton reflection (see Fig. 5, left panel).

Then, we included a reflection component with *relxillns* (García et al. 2022). The final model thus reads

$$\text{polconst}(\text{diskbb} + \text{thcomp} * \text{bbodyrad} + \text{relxillns}).$$

In *relxillns* we fixed the dimensionless spin $a = 0.2$ (assuming a typical NS spin frequency; see Braje et al. 2000) and the number density $\log n_e = 18$ (appropriate for the inner disk of a NS-LMXB; see, e.g., García et al. 2016) because these parameters are not well constrained by the fit. With the addition of the

³ https://heasarc.gsfc.nasa.gov/docs/nicer/analysis_threads/arf-rmf/

reflection component, the fit eventually achieves an acceptable value with $\chi^2/\text{d.o.f.} = 1031/962$ (see Fig. 5). The extrapolated luminosity in the 0.1–100 keV band is $7.6 \times 10^{37} \text{ erg s}^{-1}$, corresponding to an Eddington ratio of $0.28(1 + X)$, where X is the hydrogen mass fraction. The best-fitting parameters are reported in Table 3.

Finally, we conducted some tests making different assumptions regarding the polarization of the various spectral components. We fitted the data using a similar model as above, with the only difference being that each component is multiplied by a different *polconst*. The results are reported in Table 4. In these tests, we assumed that the PA of the Comptonized blackbody is perpendicular to that of the disk emission. This choice is consistent with the results obtained for Cyg X-2 (Farinelli et al. 2023) and with the hypothesis that the BL or SL is vertically extended. We also assumed that the PA of the reflection component is the same as the Comptonized blackbody. We first fixed the PD of both the disk and Comptonized component to 1%, which is consistent with the low inclination of the source; in this case, we obtain an upper limit to the PD of the reflection component of 22%. Then, we fixed the reflection PD to 10% and left only one of the other two components free to vary, obtaining upper limits of 3.4% to 3.6%. Next, we assumed a zero PD for the Comptonized component and found an upper limit of 1.7% for the disk PD. Finally, we tested a scenario consistent with the numerical simulations by Lapidus & Sunyaev (1985), namely, assuming a PD of 3% for the Comptonized plus reflected emission; in this case, we find an upper limit of 3.8% for the disk PD. We remark that all these tests provide the same goodness of fit.

4. Discussion and conclusions

The joint IXPE/NICER/*NuSTAR* observation of Ser X-1 – and especially its comparison with other NS-LMXBs observed by IXPE so far – allows us to draw interesting conclusions. Our analysis confirms the presence of a relativistic reflection component; this gives an inclination angle of 25° , which is less extreme than the values of $<10^\circ$ reported by Miller et al. (2013) and Ludlam et al. (2018) and consistent with the values reported by Cackett et al. (2010), Chiang et al. (2016a,b), Matrangola et al. (2017), and Mondal et al. (2020). The iron line requires an iron abundance of 5 times the solar one, consistent with the value obtained by Ludlam et al. (2018). From the reflection component, we also derive a disk truncation radius of the innermost stable circular orbit (ISCO) between 1.1 and 1.9, or 14–24 km assuming a canonical NS mass of $1.4 M_\odot$. This is not far from the radius of the disk blackbody component, which is found to be in the range 12–13 km for an inclination of 25° . Polarized reflected emission has been suggested as a possible explanation for the unexpectedly large polarization observed in some atolls (Saade et al. 2024; Di Marco et al. 2023a) as well as Z sources, especially when observed in the horizontal branch (Cocchi et al. 2023; Fabiani et al. 2024). However, for Ser X-1 we do not obtain a detection despite the significant reflection component.

The two atolls GS 1826–238 and GX 9+9 provide an interesting comparison with Ser X-1. GS 1826–238 has a low polarization ($< 1.3\%$) and no reflection features (Capitanio et al. 2023). GX 9+9, on the contrary, shows a significant reflection component (Iaria et al. 2020) and a PD of $\sim 2\%$ (Chatterjee et al. 2023; Ursini et al. 2023), which can be attributed to a combination of BL and reflected emission (Ursini et al. 2023). Ser X-1 is a somewhat mixed case, in that the reflected emission is significant but the X-ray polarization is relatively low ($< 2\%$). We can attribute this to the low inclination of the source. Indeed,

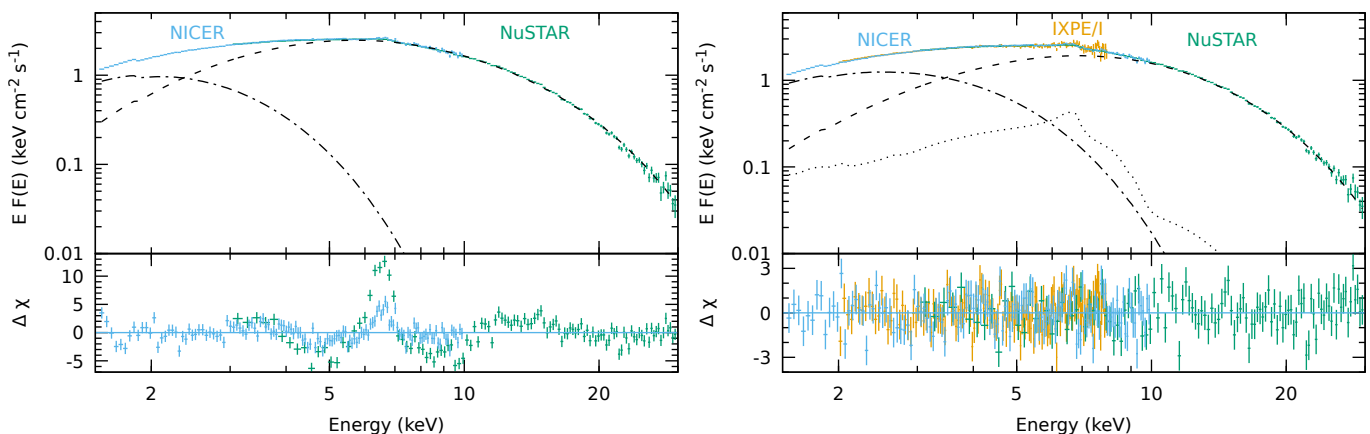


Fig. 5. Deconvolved flux spectra fitted with different models and corresponding residuals. Left panel: Model composed of `diskbb` (dash-dotted line) and `thcomp*bodyrad` (dashed line), with residuals showing the presence of reflection features. For the sake of clarity, only NICER and *NuSTAR* data are shown. Right panel: Model including `relxillns` (dotted line). The data from *NuSTAR*/FPMA and FPMB were combined (with `setplot` group in `XSPEC`) for plotting purposes only.

numerical simulations indicate that the polarization of the radiation emitted by the BL is $\lesssim 1\%$ (Gnarini et al. 2022; Farinelli et al. 2024). A low polarization is also expected for the intrinsic disk emission at low inclinations (Chandrasekhar 1960). The only other component that could produce a significant polarization is Compton reflection (Matt 1993; Poutanen et al. 1996; Schnittman & Krolik 2009). Lapidus & Sunyaev (1985) calculated the polarized fraction of X-ray-burster radiation, both during bursts and in the stationary phase, for the BL plus disk reflection. The authors found a relatively large polarization in stationary phases, even for low inclinations ($\sim 3\%$ at 25°). However, their calculations did not include the intrinsic disk emission, which in Ser X-1 accounts for 44% of the 2–8 keV photon flux (see Table 3) and can dilute the polarization. It is indeed possible to fit the data assuming a 3% PD of the BL plus reflection component, in which case the fit yields an intrinsic disk polarization lower than 3.8%.

We note that, at the accretion rate of Ser X-1 ($\sim 30\%$ of the Eddington limit; see Sect. 3.3), the BL is indeed expected to form a bright equatorial belt (Inogamov & Sunyaev 1999; Popham & Sunyaev 2001; Suleimanov & Poutanen 2006). It is reasonable to assume that a fraction of the BL emission is reflected by the disk, whose inner radius is not too far from the NS surface, and becomes polarized. However, different configurations are possible. For example, assuming the extreme case of a zero polarization of the high-energy component, we get an upper limit to the disk polarization of 1.7%, which would still indicate an inclination lower than 50° .

Finally, four type-I short X-ray bursts were detected during the observation. Their properties (occurrence, profile, and duration) are consistent with previous observations of Ser X-1 with RXTE (Galloway et al. 2008). The upper limit to the burst polarization is 80%. It might be possible to obtain better constraints on the burst polarization by stacking frequent long bursts, which tend to occur at low accretion rates (i.e., in the low hard state). Future IXPE observations of NS-LMXBs, possibly in different spectral states, will place further constraints on their average polarization properties and extend our knowledge of these sources.

Acknowledgements. This research used data products provided by the IXPE Team (MSFC, SSDC, INAF, and INFN) and distributed with additional software tools by the High-Energy Astrophysics Science Archive Research Center (HEASARC), at NASA Goddard Space Flight Center (GSFC). The Imaging X-ray Polarimetry Explorer (IXPE) is a joint US and Italian mission. FU, AG, SB, FC, and GM acknowledge financial support by the Italian Space Agency (Agen-

zia Spaziale Italiana, ASI) through contract ASI-INAF-2022-19-HH.0. SF has been supported by the project PRIN 2022 - 2022LWPEXW - “An X-ray view of compact objects in polarized light”, CUP C53D23001180006. AB acknowledges support from the Finnish Cultural Foundation grant 00240328. JP thanks the Academy of Finland grant 333112 for support.

References

- Arnaud, K. A. 1996, in ASP Conf. Ser., Vol. 101, *Astronomical Data Analysis Software and Systems V*, ed. G. H. Jacoby & J. Barnes, 17
- Asai, K., Mihara, T., & Matsuoka, M. 2022, *PASJ*, 74, 974
- Baldini, L., Bucciantini, N., Lalla, N. D., et al. 2022, *SoftwareX*, 19, 101194
- Balucinska, M. & Czerny, M. 1985, *Acta Astron.*, 35, 291
- Bhattacharyya, S. & Strohmayer, T. E. 2007, *ApJ*, 664, L103
- Bobrikova, A., Forsblom, S. V., Di Marco, A., et al. 2024, *A&A*, 688, A170
- Braje, T. M., Romani, R. W., & Rauch, K. P. 2000, *ApJ*, 531, 447
- Bult, P., Jaisawal, G. K., Güver, T., et al. 2019, *ApJ*, 885, L1
- Cackett, E. M., Miller, J. M., Ballantyne, D. R., et al. 2010, *ApJ*, 720, 205
- Cackett, E. M., Miller, J. M., Bhattacharyya, S., et al. 2008, *ApJ*, 674, 415
- Capitanio, F., Fabiani, S., Gnarini, A., et al. 2023, *ApJ*, 943, 129
- Chandrasekhar, S. 1960, *Radiative transfer* (Dover)
- Chatterjee, R., Agrawal, V. K., Jayasurya, K. M., & Katoch, T. 2023, *MNRAS*, 521, L74
- Chiang, C.-Y., Cackett, E. M., Miller, J. M., et al. 2016a, *ApJ*, 821, 105
- Chiang, C.-Y., Morgan, R. A., Cackett, E. M., et al. 2016b, *ApJ*, 831, 45
- Cocchi, M., Gnarini, A., Fabiani, S., et al. 2023, *A&A*, 674, L10
- Cornelisse, R., Casares, J., Charles, P. A., & Steeghs, D. 2013, *MNRAS*, 432, 1361
- Di Marco, A., Costa, E., Muleri, F., et al. 2022, *AJ*, 163, 170
- Di Marco, A., La Monaca, F., Poutanen, J., et al. 2023a, *ApJ*, 953, L22
- Di Marco, A., Soffitta, P., Costa, E., et al. 2023b, *AJ*, 165, 143
- Fabiani, S., Capitanio, F., Iaria, R., et al. 2024, *A&A*, 684, A137
- Farinelli, R., Fabiani, S., Poutanen, J., et al. 2023, *MNRAS*, 519, 3681
- Farinelli, R., Waghmare, A., Ducci, L., & Santangelo, A. 2024, *A&A*, 684, A62
- Galloway, D. K., Muno, M. P., Hartman, J. M., Psaltis, D., & Chakrabarty, D. 2008, *ApJS*, 179, 360
- García, J. A., Dauser, T., Ludlam, R., et al. 2022, *ApJ*, 926, 13
- García, J. A., Fabian, A. C., Kallman, T. R., et al. 2016, *MNRAS*, 462, 751
- Gnarini, A., Ursini, F., Matt, G., et al. 2022, *MNRAS*, 514, 2561
- Harrison, F. A., Craig, W. W., Christensen, F. E., et al. 2013, *ApJ*, 770, 103
- Hasinger, G. & van der Klis, M. 1989, *A&A*, 225, 79
- Iaria, R., Mazzola, S. M., Di Salvo, T., et al. 2020, *A&A*, 635, A209
- Inogamov, N. A. & Sunyaev, R. A. 1999, *Astronomy Letters*, 25, 269
- Jayasurya, K. M., Agrawal, V. K., & Chatterjee, R. 2023, *MNRAS*, 525, 4657
- Kastra, J. S. & Bleeker, J. A. M. 2016, *A&A*, 587, A151
- La Monaca, F., Di Marco, A., Poutanen, J., et al. 2024, *ApJ*, 960, L11
- Lapidus, I. I. & Sunyaev, R. A. 1985, *MNRAS*, 217, 291
- Ludlam, R. M., Miller, J. M., Arzoumanian, Z., et al. 2018, *ApJ*, 858, L5
- Masetti, N., Foschini, L., Palazzi, E., et al. 2004, *A&A*, 423, 651
- Matranga, M., Di Salvo, T., Iaria, R., et al. 2017, *A&A*, 600, A24
- Matsuoka, M., Kawasaki, K., Ueno, S., et al. 2009, *PASJ*, 61, 999
- Matt, G. 1993, *MNRAS*, 260, 663

Table 3. Best-fitting model parameters of the fits to the *NuSTAR* and *NuSTAR*+IXPE data.

Parameter	
diskbb	
kT_{in} (keV)	$0.93^{+0.01}_{-0.03}$
$R_{\text{in}} \sqrt{\cos i}$ (km)	$13.1^{+0.2}_{-0.4}$
bbodyrad	
kT_{bb} (keV)	$1.38^{+0.02}_{-0.05}$
R_{bb} (km)	$7.7^{+0.2}_{-0.5}$
thcomp	
τ	$8.1^{+0.3}_{-0.2}$
kT_{e} (keV)	$2.92^{+0.03}_{-0.04}$
relxillns	
q_{em}	2.26 ± 0.09
a	[0.2]
incl (deg)	$25.1^{+1.3}_{-1.5}$
R_{in} (units of R_{ISCO})	$1.6^{+0.3}_{-0.5}$
kT_{bb} (keV)	[$=kT_{\text{bb,bbodyrad}}$]
$\log(\xi/\text{erg cm s}^{-1})$	2.88 ± 0.07
A_{Fe}	$5.0^{+1.1}_{-0.3}$
$\log n_{\text{e}}$	[18]
N_{r} (10^{-3})	$1.37^{+0.09}_{-0.08}$
Cross-calibration	
$C_{\text{DU1-FPMA}}$	$0.881^{+0.005}_{-0.007}$
$C_{\text{DU2-FPMA}}$	$0.880^{+0.006}_{-0.005}$
$C_{\text{DU3-FPMA}}$	$0.861^{+0.005}_{-0.006}$
$C_{\text{FPMB-FPMA}}$	0.987 ± 0.001
$C_{\text{XTI-FPMA}}$	0.929 ± 0.001
Gain shift	
α_{DU1}	$1.013^{+0.002}_{-0.003}$
β_{DU1} (eV)	-53^{+12}_{-10}
α_{DU2}	$1.008^{+0.002}_{-0.003}$
β_{DU2} (eV)	-30^{+12}_{-11}
α_{DU3}	$1.007^{+0.002}_{-0.003}$
β_{DU3} (eV)	-33^{+12}_{-11}
α_{XTI}	1.032 ± 0.001
β_{XTI} (eV)	-65^{+2}_{-3}
$\chi^2/\text{d.o.f.}$	1031/962
Photon flux ratios ^a	
2–8 keV	
$F_{\text{diskbb}}/F_{\text{tot}}$	0.44
$F_{\text{bbodyrad}}/F_{\text{tot}}$	0.47
$F_{\text{relxillns}}/F_{\text{tot}}$	0.09
2–4 keV	
$F_{\text{diskbb}}/F_{\text{tot}}$	0.58
$F_{\text{bbodyrad}}/F_{\text{tot}}$	0.35
$F_{\text{relxillns}}/F_{\text{tot}}$	0.07
4–8 keV	
$F_{\text{diskbb}}/F_{\text{tot}}$	0.19
$F_{\text{bbodyrad}}/F_{\text{tot}}$	0.69
$F_{\text{relxillns}}/F_{\text{tot}}$	0.12
Energy flux (2–8 keV)	
F_{tot} ($\text{erg s}^{-1} \text{cm}^{-2}$)	5.1×10^{-9}

Notes. Uncertainties are given at the 68% confidence level for one parameter of interest. Parameters in square brackets were kept frozen during the fit. The normalizations of *diskbb* and *bbodyrad* are computed assuming a source distance of 7.7 kpc.

^(a) The photon fluxes are in units of $\text{photon cm}^{-2} \text{s}^{-1}$.

Table 4. PD and PA of each spectral component for different scenarios.

Component	PD (%)	PA (deg)
<i>diskbb</i>	[1]	$=\text{PA}_{\text{bbodyrad}} - 90$
<i>thcomp*bbodyrad</i>	[1]	(unconstrained)
<i>relxillns</i>	< 22	$=\text{PA}_{\text{bbodyrad}}$
<i>diskbb</i>	[1]	$=\text{PA}_{\text{bbodyrad}} - 90$
<i>thcomp*bbodyrad</i>	< 3.4	(unconstrained)
<i>relxillns</i>	[10]	$=\text{PA}_{\text{bbodyrad}}$
<i>diskbb</i>	< 3.6	$=\text{PA}_{\text{bbodyrad}} - 90$
<i>thcomp*bbodyrad</i>	[1]	(unconstrained)
<i>relxillns</i>	[10]	$=\text{PA}_{\text{bbodyrad}}$
<i>diskbb</i>	< 1.7	$=\text{PA}_{\text{bbodyrad}} - 90$
<i>thcomp*bbodyrad</i>	[0]	-
<i>relxillns</i>	[10]	(unconstrained)
<i>diskbb</i>	< 3.8	$=\text{PA}_{\text{bbodyrad}} - 90$
<i>thcomp*bbodyrad</i>	[3]	(unconstrained)
<i>relxillns</i>	[3]	(unconstrained)

Notes. Upper limits are reported at 99% confidence level for one interesting parameter ($\Delta\chi^2 = 6.63$). Parameters in square bracket are frozen.

Miller, J. M., Parker, M. L., Fuerst, F., et al. 2013, *ApJ*, 779, L2
Mitsuda, K., Inoue, H., Koyama, K., et al. 1984, *PASJ*, 36, 741
Mondal, A. S., Dewangan, G. C., & Raychaudhuri, B. 2020, *MNRAS*, 494, 3177
Oosterbroek, T., Barret, D., Guainazzi, M., & Ford, E. C. 2001, *A&A*, 366, 138
Piconcelli, E., Jimenez-Bailón, E., Guainazzi, M., et al. 2004, *MNRAS*, 351, 161
Popham, R. & Sunyaev, R. 2001, *ApJ*, 547, 355
Poutanen, J., Nagendra, K. N., & Svensson, R. 1996, *MNRAS*, 283, 892
Saade, M. L., Kaaret, P., Gnarini, A., et al. 2024, *ApJ*, 963, 133
Sánchez-Fernández, C., Kajava, J. J. E., Poutanen, J., Kuulkers, E., & Suleimanov, V. F. 2020, *A&A*, 634, A58
Schnittman, J. D. & Krolik, J. H. 2009, *ApJ*, 701, 1175
Soffitta, P., Baldini, L., Bellazzini, R., et al. 2021, *AJ*, 162, 208
Suleimanov, V. & Poutanen, J. 2006, *MNRAS*, 369, 2036
Sztajno, M., Basinska, E. M., Cominsky, L. R., Marshall, F. J., & Lewin, W. H. G. 1983, *ApJ*, 267, 713
Ursini, F., Farinelli, R., Gnarini, A., et al. 2023, *A&A*, 676, A20
van Paradijs, J. & Lewin, H. G. 1986, *A&A*, 157, L10
Weisskopf, M. C., Soffitta, P., Baldini, L., et al. 2022, *JATIS*, 8, 026002
Wilms, J., Allen, A., & McCray, R. 2000, *ApJ*, 542, 914
Worpel, H., Galloway, D. K., & Price, D. J. 2013, *ApJ*, 772, 94
Worpel, H., Galloway, D. K., & Price, D. J. 2015, *ApJ*, 801, 60
Zdziarski, A. A., Szanecki, M., Poutanen, J., Gierliński, M., & Biernacki, P. 2020, *MNRAS*, 492, 5234

Table A.1. Spectral parameters at the peak for each burst.

Burst	$kT_{\text{bb,peak}}$ (keV)	$R_{\text{bb,peak}}$ (km)	$F_{\text{bb,peak}}$ (10^{-9} erg s $^{-1}$ cm $^{-2}$)	$\chi^2/\text{d.o.f.}$
1	$1.92^{+0.13}_{-0.12}$	8.2 ± 0.6	16 ± 3	89/73
2	$1.95^{+0.16}_{-0.14}$	$8.4^{+1.3}_{-1.1}$	18.4 ± 1.5	53/46
3	$2.10^{+0.19}_{-0.16}$	7.3 ± 1.1	19.7 ± 1.7	48/42
4	$2.00^{+0.14}_{-0.12}$	$9.7^{+1.2}_{-1.1}$	27.3 ± 1.8	52/52

Appendix A: Spectral analysis of the bursts

To perform a time-resolved spectral analysis of the bursts, we extracted the spectra within intervals of 1 s, covering the duration of the bursts. We fitted the data subtracting the persistent emission as background. This standard procedure is based on the assumption that the persistent emission does not change in the burst phase, which is often a good approximation (e.g., [van Paradijs & Lewin 1986](#), [Galloway et al. 2008](#)). We modeled the burst emission with a simple blackbody. We have also attempted more sophisticated treatments, such as scaling the background with a free constant (e.g., [Worpel et al. 2013, 2015](#); [Sánchez-Fernández et al. 2020](#)) or including a further reflection component (e.g., [Bult et al. 2019](#)). However, the fits are not improved and the free parameters become poorly constrained.

The results are summarized in [Table A.1](#). The peak temperature of each burst is around 2 keV. The peak blackbody radius is 8–9 km assuming a distance of 7.7 kpc, and we do not find evidence for photospheric radius expansion. The average peak flux is $(20 \pm 2) \times 10^{-9}$ erg s $^{-1}$ cm $^{-2}$, consistent with the value reported for this source by [Galloway et al. \(2008\)](#).